On high-performance rotational energy harvesting with a novel cam-like dielectric elastomer generator

Shitong Fang[1,2], Shuaibo Wang[1,2], Guoqing Zhang[1,2], Chen Wang[1,2], Junchen Xu[1,2], ZhouzhouWang[1,2], Aijie Feng[1,2], Zijian Qiao[3], Daniil Yurchenko[3], Zhihui Lai [1,2,*]

[1] Shenzhen Key Laboratory of High Performance Nontraditional Manufacturing, College of Mechatronics and Control Engineering, Shenzhen University, Shenzhen 518060, P. R. China

[2] Guangdong Key Laboratory of Electromagnetic Control and Intelligent Robots, College of Mechatronics and Control Engineering, Shenzhen University, Shenzhen, 518060, P. R. China

[3] School of Mechanical Engineering and Mechanics, Ningbo University, Ningbo 315211, P. R. China

[4] Institute Sound and Vibration Research, University of Southampton, Southampton, SO17 1BJ, UK

[*] Corresponding author: Zhihui Lai (laizh@szu.edu.cn)

Abstract: Rotational energy is a type of common energy sources that can be harvested for supplying low-powered electronic devices. This paper proposes and investigates a novel cam-like dielectric elastomer generator (CDEG) for rotational energy harvesting with high performance. A mushroom-head clamp is designed to form a type of advanced conical dielectric elastomer membranes (DEMs). Moreover, a type of multi-protrusion cam mechanisms is designed in the CDEG for effectively converting any external rotational excitation into the linear reciprocating motion, which can be further converted into electricity through the DEMs. Firstly, the operational principle of the system under external rotational excitations is analyzed via the theoretical model of the deformation of DEMs and their electrical output. Secondly, the prototype is fabricated and the rotational-linear motion conversion rule of its cam-like mechanism and the DEM capacitance calculation approach are validated. Experimental results show that adequate charging time and discharging time of the DEMs, which can be realized through the proposed cam-like mechanisms, are beneficial to the energy harvesting (EH) performance of the system. Thirdly, with the validated theoretical model, numerical simulations are conducted to further study the system dynamics and the influences of important system parameters on the EH performance, so as to provide a guideline for the system improvement. Finally, the Genetic algorithm is adopted to obtain the optimal system parameters and the corresponding electrical output of the proposed CDEG, demonstrating its superior output power at ultra-low rotational frequencies compared with other typical rotational energy harvesters in literature.

Keywords: Rotational energy harvesting; dielectric elastomer generator; cam-like mechanism; rotational-linear conversion; theoretical model

1. Introduction

In recent years, with the rapid development of Internet of things technology, the wireless sensors, portable electronic devices, micro robots, etc., have been applied in an increasing number of application scenarios [1]. The common energy supply solution for these electronic devices is the chemical battery. However, the battery has shortcomings including limited service life, requirements of frequent replacement and maintenance as well as environmental pollutions. Therefore, harvesting energy from the operation environments of small-scale electronic devices

to power these devices has become a viable alternative to the batteries [2-4]. So far, the solar energy [5], wind energy [6, 7], tidal energy [8], human motion energy [9], vibrational energy [10-13], rotational energy [14-18], etc., have been utilized for electrical energy generation. Among these energy sources, the rotational energy is ubiquitous in the living and natural environment including car wheels, drones engines, wind mills, water wheels, etc [19, 20]. Therefore, the research on rotational energy harvesting has received massive attentions in recent years.

Researchers have proposed various small-scale rotational energy harvesters based on different electromechanical conversion mechanisms including the electromagnetic (EM) [21, 22], piezoelectric (PE) [23, 24], triboelectric (TE) [25, 26] and electrostatic (ES) [27]. Among these, although the EM generators enjoy the ease of manufacture, higher structural robustness due to the high durability of their two main constitutes of coils and magnets [28-30]. However, their energy output at low excitation frequencies is subjected to the scaling effect, thus limiting the ease of integration [31]. The PE generators generally have the advantages of high energy densities and the ease of integration with small-scale electronics, whereas the commonly used PE material, lead zirconate titanate, is brittle and may easily break under too large strain [32-34]. Although other PE materials such as polyvinylidene fluoride can sustain the larger strain, they commonly possess the lower piezoelectric constants and generate the lower energy output [35]. In the past decades, the TE generators have been developed rapidly, which use both the principles of frictional electrification and electrostatic induction to generate electrical energy [36, 37]. Compared with the EM and PE generators, their remarkable feature is the superior energy harvesting performance under low-frequency and low-amplitude excitations. However, this is at the expense of the frequent contact and friction processes between materials, which may cause the component failure and the reduction of system reliability. As for the ES generators, as the essentially variable capacitors [38, 39], they can be polarized when a direct-current power is applied to the two plates [40] or the electret materials [41, 42]. The distance or relative position of the two plates changes under the external excitations, thus causing the capacitance variation and converting external mechanical energy into electrical energy. The traditional ES generators are insensitive to the excitation frequencies and amplitudes [43], whereas their applications are still limited due to the relatively low energy density resulting from the low dielectric permittivity of air [44].

In recent years, a new type of ES generators called dielectric elastomer generators (DEGs) has been proposed and studied. The pioneer work was conducted by Pelrine *et al.* [45] in 2001, who proposed the DEG that consists of a relatively soft polymer sandwiched between two compliant electrodes. Compared with other generators, DEGs have the advantages including: (1) high energy conversion efficiency that is rather independent of operation frequencies [46], (2) ease of fabrication and installation, (3) high impact and corrosion resistance [47], (4) good impedance matching to abundant energy sources [45], and (5) low fabrication cost [48]. Therefore, DEGs have attracted widespread attentions from the scientific community.

Up to now, various DEGs have been proposed to harvest energy from different energy sources. For example, researchers have proposed DEGs for ocean wave energy harvesting including the pressure differential wave energy converters (WECs) designed by Righi *et al.* [49], and the WECs that combine the concept of the oscillating water columns with the DEG designed by Moretti *et al.* [50]. McKay *et al*. [51] proposed an integrated generator with self-

priming characteristic to harvest the vibrational energy. Kornbluh *et al.* [52] designed a heel impact DEG to harvest the energy of human movement. Yurchenko and his co-workers [53, 54] have designed a vibro-impact DEG (VI DEG) to harvest vibrational energy through the impacts between a rigid small ball and the DE membranes. Later, this model was further used to harvest wind energy by embedding it into a bluff body [55, 56]. However, there are few studies focus on the DEGs for rotational energy harvesting, which is potential due to the fact that rotational energy sources are abundant and the DEGs has good impedance matching to them. So far, Jean-Mistral *et al.* [57] and Armbruster *et al.* [58] proposed two different DEGs that can harvest energy from the bending motion of human knee joints. Fan *et al.* [59] proposed a dielectric elastomer pendulum (DEP) device to harvest the swing energy. However, these DEGs focus on harvesting the energy from intermittent rotational motions. For energy harvesting from continuous rotations, Vu-Cong *et al*. [60] used a crank and connecting rod mechanism to investigate the energy conversion performance of the DE material, whereas this work was not used in actual DEG models. Zhang and his co-workers [44, 61] attached the VI DEG onto a wind turbine to harvest the wind-induced rotations. However, these wind energy harvesting devices have relatively large scales, which limit their application scenarios. Later, Zhang *et al.* [62] proposed a small-scale DEG with a crank-connecting rod mechanism that can be used for rotational energy harvesting, whereas it is relatively complex with low stability and reliability. In summary, the DEGs provide a potential solution for high-performance energy harvesting from different energy sources, whereas the mechanical modulation methods for rotational energy harvesting still need to be explored.

In order to make full use of the superiority of the DE material to harvest energy from ubiquitous rotational excitations, a cam-like DEG (CDEG), which involves a newly designed multi-protrusion cam mechanism that can convert any rotation types into a linear reciprocating motion, has been proposed in this work. The proposed mechanism is aimed at achieving the highly efficient rotational energy harvesting. The rest of this paper is organized as follows. Section 2 introduces the specific design process of the CDEG system. Section 3 analyzes the working principle of the system in detail with the theoretical model of both mechanical and electrical parts. Section 4 presents the experimental verification of the theoretical model and analysis. In Section 5, the energy harvesting (EH) performance of the system is studied through numerical simulation, and the influences of the rotation frequency, the structural parameters, the DEM's pre-stretch ratio, and the initial input voltage on the system EH performance are investigated. Section 6 summarizes the key conclusions.

2. Design of the cam-like DEG for rotational energy harvesting

2.1 Layout design of the dielectric elastomer membrane and the clamps

A DEG can generate electricity through the regular capacitance change of the dielectric elastomer membranes (DEMs) during their stretching-recovering processes. Hence, the layout of the DEM and its potential deformation mode, which have significant influences on the EH performance, should be considered first. Among various topologies of DEMs, the circular DEM with its center clamped to rigid discs as shown in Fig. 1(a), which has been used to assemble a conical DEG [63], is preferred due to its ease of implementation and high energy density [64]. It can be observed that the conventional conical DEM is a uniformly pre-stretched annular

membrane at its initial state. Its external perimeter is clamped between two identical fixed ring frames, and its inner perimeter is fixed between two identical rigid disc-type clamps. With this configuration, the longitudinal forces are applied to the rigid discs so that the DEM can be deformed to a conical configuration.

However, it can be observed that when the DEM is under the out-of-plane deformation, it will be subjected to concentrated stress around the rigid discs, leading to the risk of break during periodic deformation-recovery processes. In order to improve the service life and the energy harvesting performance of the DEM, a new design of the mushroom-head clamp is introduced to replace one of the disk-type clamps, as shown in Fig. 1(b). It can be seen that when a longitudinal force is applied to the clamps, the DEM will be deformed smoothly without the loss of contact with the mushroom-head clamp, thus avoiding the stress concentration and mechanical failure. Moreover, the mushroom-head clamp is beneficial to enhancing the capacitance change of the DEM during the deformation-recovery process and therefore improving the energy harvesting performance, which will be demonstrated later in Section 4.3. It should be noted that as the DEM in this work is assumed to be subjected to the unidirectional deformation, only one mushroom-head clamp is used. Two symmetrical installed mushroom-head clamps for the DEM would be helpful when the DEM can be deformed in both directions.

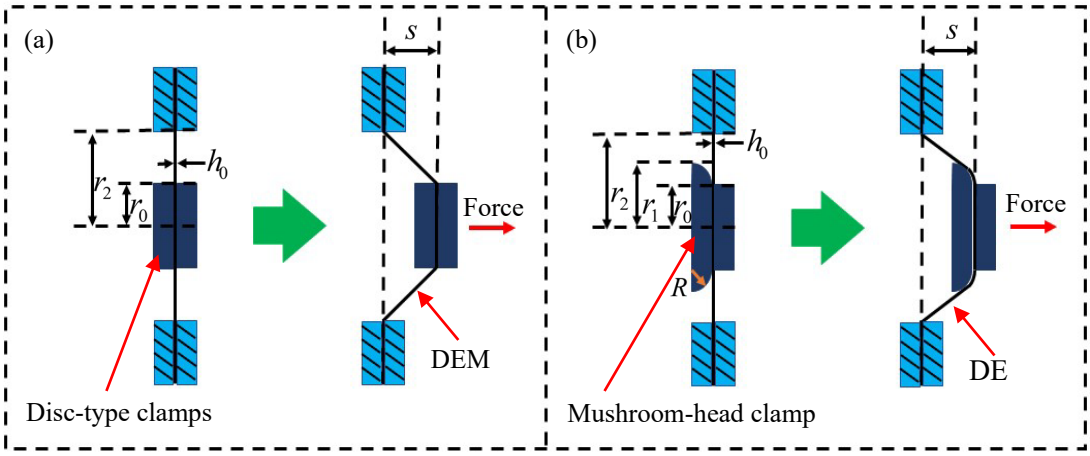

Fig. 1 The layouts of the clamps and the DEM at its initial state and deformed state. (a) The conventional conical DEM with two identical rigid disc-type clamps; (b) the developed conical DEM with a disc-type clamp and a proposed mushroom-head clamp.

2.2 Design of the rotational-linear motion conversion mechanism

With the developed conical DEM, a DEG can generate electricity when they are subjected to external force or excitation. This is achieved through the regular capacitance change of the DEMs during their regular stretching-recovering processes. However, this type of DEMs can be only deformed and recovered under a linear reciprocating motion, whereas hardly deformed by a rotational excitation directly. In order to take advantages of this type of DEMs to harvest rotational energy, a feasible way is to convert the rotational motion into the linear reciprocating motion. The mechanisms that can realize this mainly include the crank linkage mechanism and the cam mechanism. The structure of the crank linkage mechanism is relatively complicated, resulting in high mechanical energy losses and low energy harvesting efficiencies. By comparison, the cam mechanism can convert the rotational motion of a cam into the linear reciprocating motion of its follower, and possesses the advantages of simple structure,

compactness, convenient design, *etc*. Moreover, the follower of cam can realize almost any expected movements according to the profile of cam. Therefore, the cam mechanism is designed for the DEG to harvest ubiquitous rotational energy from ambient environments, such as automobiles, windmills, and other rotating machinery.

A traditional cam mechanism, which indicates a circular cam hinged off-axis, as shown in Fig. 2(a), consists of a cam, a follower, and a frame. When a constant-speed rotation is applied to the cam, the follower of cam can move with different motion laws commonly including the uniform motion, simple harmonic motion, and sine acceleration motion. It is apparent that the motion laws of the follower are decided by the cam profiles. For the uniform motion, the follower of cam may be suffered from a strong rigid impact at the sudden increase of rotation frequency, thus causing serious mechanical failure. Hence, this type of motion is more suitable for low-speed rotations. While for the sine acceleration motion, the inertial force is relatively large, and the high machining accuracy of cam profile is required. Therefore, the simple harmonic motion law, which is more suitable for low/medium speed rotations, is designed in this paper.

Besides the expected motion law, another factor that should be taken into account is the size of cam, which is decided by the pressure angle α_p (as shown in Fig. 2(a)), that is, the angle between the driving force acting on the follower and the moving direction of the follower. It is noted that the pressure angle varies during the rotation of cam. The largest pressure angle $\alpha_{p\max}$ should not exceed the allowable pressure angle $[\alpha_p]$, which is recommended as 30° for a normal straight-moving cam mechanism [65]. The largest pressure angle for a cam mechanism with simple harmonic motion can be written as:

$$\alpha_{p\max} = \arctan\frac{\pi H}{2r\delta\sqrt{1+\dfrac{H}{r}}} \tag{1}$$

where H is the lifting distance of the cam, r is the prime circle radius, and δ the lifting angle. It can be observed from Eq. (1) that when other parameters are given, a larger $\alpha_{p\max}$ will lead to a smaller value of r. Hence, in order to design a cam mechanism as small as possible, the largest pressure angle $\alpha_{p\max}$ should be set as large as possible in the design process. Therefore, it can be set to equal to $[\alpha_p]$.

For the traditional cam mechanism shown in Fig. 2(a), a complete circle of the cam will produce a period of linear reciprocating motion of the follower, thus resulting in an energy harvesting cycle for the DEM. In this paper, a novel cam-like mechanism involving a cam with N protrusions is further developed, as shown in Fig. 2(b)-(d). For this cam-like mechanism, when the cam rotates in one cycle, the follower produces N periods of linear reciprocating motions, and therefore the DEM can realize N energy harvesting cycles. Thus, the energy output of the DEG can be further improved. Moreover, the cam-like mechanism is able to keep the system dynamic balance under rotational excitations due to its structural symmetry, which is another improvement aspect of this structure.

A four-protrusion cam structure is first designed, as shown in Fig. 2(b). The lifting distance of this cam for each protrusion is H; the lifting and lowering angles are δ and δ',

respectively; the prime circle radius is r, which can be calculated according to Eq. (1) when the parameters H, δ and $\alpha_{p\max}$ are given. Thus, when the cam rotates in one cycle, the follower of cam will move back and forth for four times without staying in both the furthest and closest positions relative to the cam. Fig. 2(c) shows a three-protrusion cam structure with the same values of H and r compared to the four-protrusion one shown in Fig. 2(b). It can be seen that this cam has a larger lifting angle δ compared to the four-protrusion cam, hence, it has a smaller value of the largest pressure angle $\alpha_{p\max}$. Fig. 2(d) shows another three-protrusion cam structure with the same values of H and r, while the values of δ and δ' are set to be the same as those of the four-protrusion cam shown in Fig. 2(b), which are larger than those of the three-protrusion cam shown in Fig. 2(c). Hence, the cam has extra cam angles of outer dwell (δ_s) and inner dwell (δ_s') for each protrusion. This design enables the follower to stay for a certain duration both in its furthest and closest positions relative to the cam when it moves back and forth, thus providing extra charging time and discharging time for the DEMs at its largest deformation and original condition, respectively. This special design is beneficial to enhancing the energy harvesting performance of the DEM during the deformation-recovery process, which will be demonstrated later in Section 4.4. It is noted that as the follower always keeps direct contact with the cam, the cam profiles shown in Fig. 2(b)-(d) are obtained through a graphical method based on the expected simple harmonic motion type.

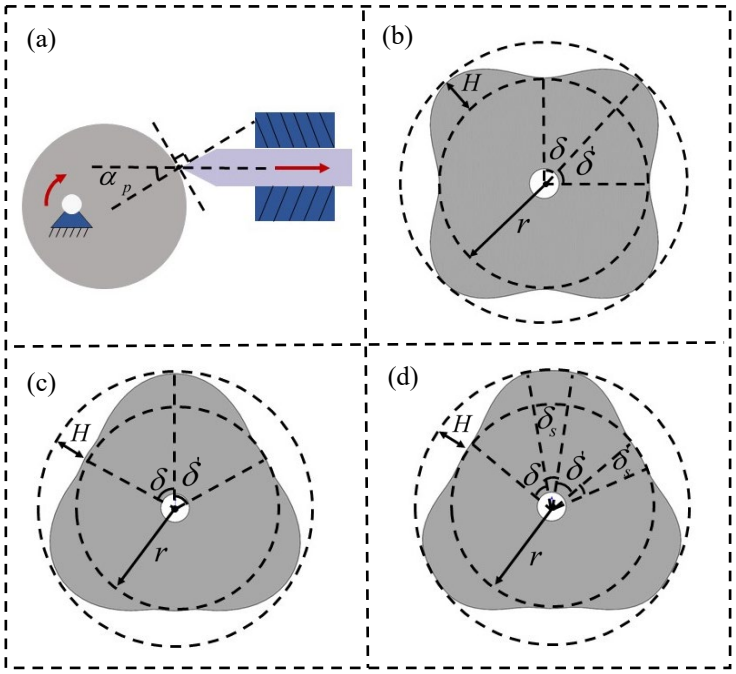

Fig. 2 The schematics of (a) the traditional cam, (b) the four-protrusion cam, (c) the three-protrusion cam, and(d) the three-protrusion cam with extra cam angles for outer dwell and inner dwell.

2.3 Overall design of the cam-like DEG for rotational energy harvesting

With the help of a proposed multi-protrusion cam, a novel cam-like DEG (CDEG) is further designed in this paper for rotational energy harvesting, as shown in Fig. 3. The system has a symmetrical structure with a cube shell, a cam-like mechanism with one multi-protrusion cam, and a pair of symmetrically installed followers, push rods, end caps, disc-shaped clamps,

mushroom-head clamps, annular-shaped clamps, and circular DEMs on both sides. The cam is installed in the center of the system with its rotating shaft connected to the cube shell. There is one push rod on each side of the cam. The push rods are equipped with a roller to reduce the friction between the cam and the push rods, therefore extending the service life of the device. For each push rod, a spring is designed to wrap around it with one side fixed to the end cap and the other side moving following the push rod, thus ensuring that the roller contacts with the cam without loss. This is especially important when the restoring force of the membrane is not large enough to push the rod back. The push rod is designed as a stair-stepping cylinder, which matches the stair-stepping circular hole in the center of the end cap, so as to fix the push rod in the circumferential direction. The hollow end caps can be fixed to the cube shell through bolts on each side, while the annular-shaped clamps are fixed to the other side of the end caps with a pre-stretched DEM clamped between them and the end caps. Each DEM is clamped at its center with two clamps including a disc-shaped one and a mushroom-head one, the latter of which is fixed on the push rod. Through this configuration, the DEMs can be deformed smoothly when they are pushed by the rods through the mushroom-head clamps. The exposed annular parts of the DEMs are then sandwiched between two flexible electrodes on both ends, which are connected to the input power supply and the EH circuit.

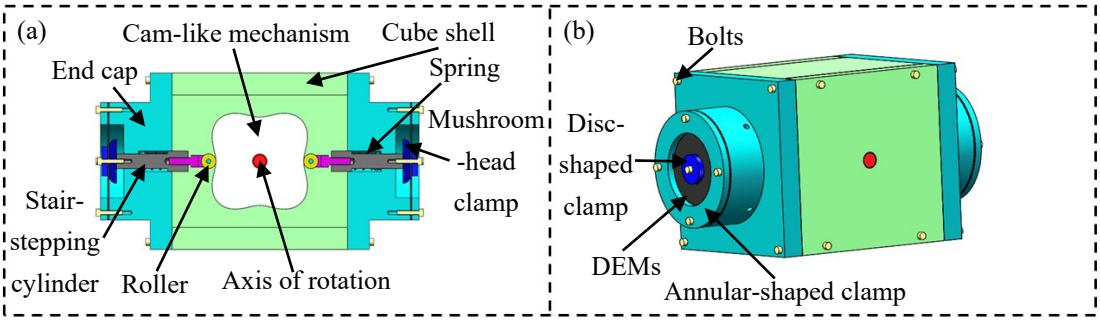

Fig. 3 The schematic of the proposed CDEG. (a) The section view; (b) the overall view.

The operational principle of the CDEG is as follows. When the cam is excited to rotate, both rods exhibit a linear reciprocating motion, thus pushing both peripherally DEMs to be deformed and recovered regularly. During this process, the capacitances of the DEMs change accordingly, and electricity can be generated in each deformation-recovery cycle. Hence, any forms of rotational energies can be converted into the electrical ones through the proposed CDEG.

3. Theoretical model and analysis

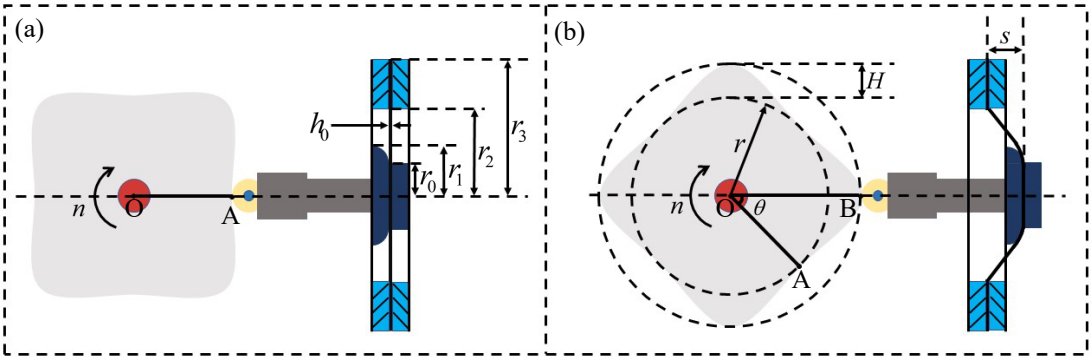

Fig. 4 (a) The initial state of the DEM and (b) the deformed state of the DEM at the largest displacement of the cam.

The energy harvesting process of the proposed CDEG is analyzed theoretically in this section through the modeling of system dynamics and electrical outputs. Here, considering that the CDEG is symmetrical, only the right part of the cam-like mechanism is analyzed as representative, as shown in Fig. 4. It should be noted that a four-protrusion cam is presented in Fig. 4 for better understanding, whereas the following analyses are applicable to other multi-protrusion cam structures as well.

Fig. 4(a) shows the initial state of the cam-like mechanism when the roller contacts the position at the minimum radius of the cam, which is denoted as point A. At this state, the pre-stretched DEM is in its original in-plane condition with radius r_2 and thickness h_0. When the roller contacts the position at the maximum radius of the cam, which is denoted as point B, the pre-stretched DEM has the largest deformation as shown in Fig. 4(b). It can be observed that the center deflection of the DEM varies as the cam rotates, the largest value $s_{\max}$ equals to the lifting distance of the cam H, i.e., $s_{\max} = H$.

Without loss of generality, the cam is assumed to rotate clockwise with a constant rotation frequency of n (Hz) or $\omega = 2\pi n$ (rad/s). Thus, the rotation angle can be calculated as $\theta(t) = \int_0^t \omega dt = \int_0^t 2\pi n dt = 2\pi n t$. It can be easily understood from Fig. 4 that the DEM is deformed based on the variance of its center deflection s, which is also the displacement of the follower and depends on the rotation angle $\theta(t)$ of the cam. With the assumption that the motion law of the follower is the simple harmonic, the relation between the follower displacement and the cam rotation angle $\theta(t)$ can be written as:

$$s(t) = \begin{cases} \dfrac{H}{2}\left(1-\cos\dfrac{\pi}{\delta}\theta(t)\right) & 0 \le \theta(t) < \delta \\ H & \delta \le \theta(t) < \delta + \delta_s \\ \dfrac{H}{2}\left[1+\cos\dfrac{\pi}{\delta'}\left(\theta(t)-\delta-\delta_s\right)\right] & \delta+\delta_s \le \theta(t) < \delta+\delta_s+\delta' \\ 0 & \delta+\delta_s+\delta' \le \theta(t) < \delta+\delta_s+\delta'+\delta_s' \end{cases} \tag{2}$$

Corresponding to Eq. (2), when $s > 0$, the DEM is deformed under the smooth contact of the mushroom-head clamp as shown in Fig. 5. At this time, the effective surface of the DEM, which indicates the annular surface of the deformed DEM coated with compliant electrodes, can be divided into two parts. The first part is in contact with a partial side of the mushroom-

head clamp; the other part forms as a conical shape. The areas of these two parts are denoted as A_1 and A_2, respectively, and their values can be calculated as:

$$\begin{cases} A_1 = 2\pi R^2\left(1-\cos\alpha\right) + 2\pi r_0 R\left[\dfrac{\pi}{2} - \sin^{-1}\left(\cos\alpha\right)\right] \\ A_2 = \pi\left(r_2 + r_0 + R\sin\alpha\right)\sqrt{\left[s - R\left(1-\cos\alpha\right)\right]^2 + \left[r_2 - r_0 - R\sin\alpha\right]^2} \end{cases} \tag{3}$$

Here, as shown in Fig. 4(a) and Fig. 5(a), r_0 is the radius of the upper surface of the mushroom-head clamp, which is equal to the radius of the disc-shaped clamp; r_1 is the radius of the lower surface of the mushroom-head clamp; r_2 is the inner radius of the annular-shaped clamp; $R = r_1 - r_0$ is the radius of the arc side of the mushroom-head clamp; α is the angle between the generatrix of A_2 and the parallel surfaces of the mushroom-head clamp, which can be calculated as [54]:

$$\alpha = \cos^{-1}\left\{\frac{-R\left(s-R\right) + r_2\sqrt{r_2^2 + s^2 - 2sR}}{\left[r_2^2 + \left(s-R\right)^2\right]}\right\} \tag{4}$$

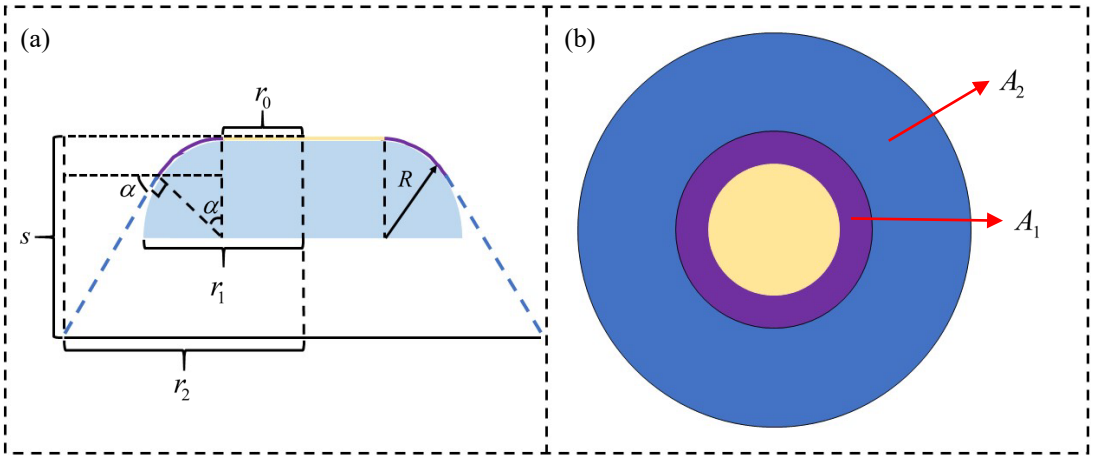

Fig. 5 (a) The section view and (b) the top view of the stretched DEM.

Thus, the effective area of the deformed DEM can be obtained by:

$$A = A_1 + A_2 \tag{5}$$

It is noted that at the initial state of the DEM, its effective area is $A_0 = \pi\left(r_2^2 - r_0^2\right)$. Assume that the effective area of the DEM is deformed uniformly, the thickness of the DEM varies as its area changes, and can be calculated as:

$$h = \frac{Vol}{A} \tag{6}$$

where $Vol = \pi A_0 h_0$ is the volume of the effective DEM, which keeps unchanged during the deformation of the DEM due to its incompressibility.

Thus, the time-varying capacitance of the DEM can be expressed as:

$$C\left(t\right) = \frac{\varepsilon_0\varepsilon_r A\left(t\right)}{h\left(t\right)} = \frac{\varepsilon_0\varepsilon_r A(t)^2}{\pi(r_2^2 - r_0^2)h_0} \tag{7}$$

where $\varepsilon_0 = 8.854187817 \times 10^{-12}$ F/m represents the vacuum dielectric constant and ε_r denotes the relative dielectric constant of the DEM.

It can be seen that the capacitance C of the DEM varies as the value of its effective area A changes, which is decided by the displacement of the follower. When the DEM is at its initial state as shown in Fig. 4(a), the DEM has its minimum capacitance as well, which can be written as:

$$C_{\min} = \frac{\pi \varepsilon_0 \varepsilon_r (r_2^2 - r_0^2)}{h_0} \tag{8}$$

When the displacement of the follower reaches its high limit as shown in Fig. 4(b), the DEM will reach its largest deformation. In this case, the effective area can be written as:

$$A_{\max} = (A_1 + A_2)\big|_{s=H} \tag{9}$$

Thus, the largest capacitance of the DEM can be obtained as:

$$C_{\max} = \frac{\varepsilon_0 \varepsilon_r A_{\max}^2}{\pi (r_2^2 - r_0^2) h_0} \tag{10}$$

When the CDEG is connected to an energy harvesting circuit [66] shown in Fig. 6(a), each DEM can harvest energy during its deformation-recovery process based on the constant charge mode [67] as shown in Fig. 6(b).

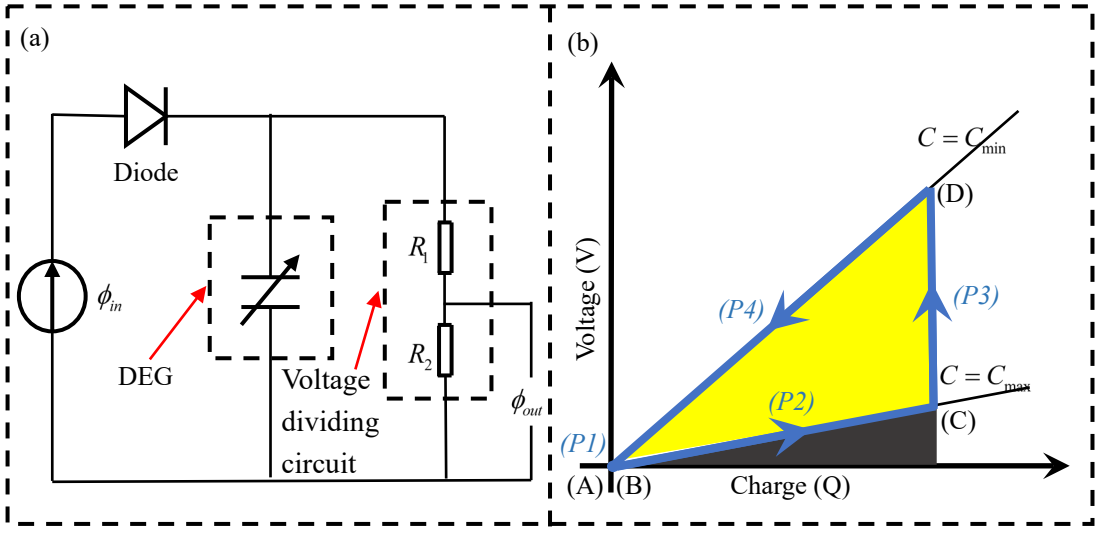

Fig. 6 (a) The energy harvesting circuit connected to the CDEG and (b) the energy harvesting scheme during one deformation-recovery process of each DEM.

It can be observed that an input voltage is applied to both DEMs and they can be charged with a total amount of charges $Q(t) = \phi_{in} C(t)$. Whenever the capacitance of the DEM drops from its maximum value to its minimum one, a output voltage peak can be produced and calculated as:

$$\phi_{out} = \frac{Q_{\max}}{C_{\min}} = \phi_{in} \frac{C_{\max}}{C_{\min}} = \phi_{in} \frac{A_{\max}^2}{\pi^2 (r_2^2 - r_0^2)^2} \tag{11}$$

The energy gained in one energy harvesting cycle of the right DEM can be further calculated as according to Fig. 6(b):

$$W_r = \frac{1}{2}C_{\min}\phi_{out}^2 - \frac{1}{2}C_{\max}\phi_{in}^2 = \frac{1}{2}\varepsilon_0\varepsilon_r\phi_{in}^2\left[\frac{A_{\max}^4 - \pi^2(r_2^2 - r_0^2)^2 A_{\max}^2}{\pi^3(r_2^2 - r_0^2)^3 h_0}\right] \tag{12}$$

Thus, the total electrical energy generated by both DEMs during a given time period (t_0 - t_1) can be written as:

$$W_{total} \approx (t_1 - t_0)nN(W_r + W_l) \tag{13}$$

Here, N is the number of the adopted cam protrusions; W_l, the value of which equals to that of W_r, is the electrical energy generated by the left DEM in each cycle.

Finally, the output power of the system during the given time period can be obtained as:

$$P_{sys} = \frac{W_{total}}{t_1 - t_0} = nN(W_r + W_l) \tag{14}$$

4. Experimental verifications

In order to verify the theoretical model and analyses of the proposed CDEG in Section 3, experimental work is conducted in this section. The experiments include validating the rotational-linear motion conversion rule of the cam-like mechanism, the capacitance of the DEM under deformation, and the output voltage of the system under external excitations.

4.1 Validation on the rotational-linear motion conversion rule of the cam-like mechanism

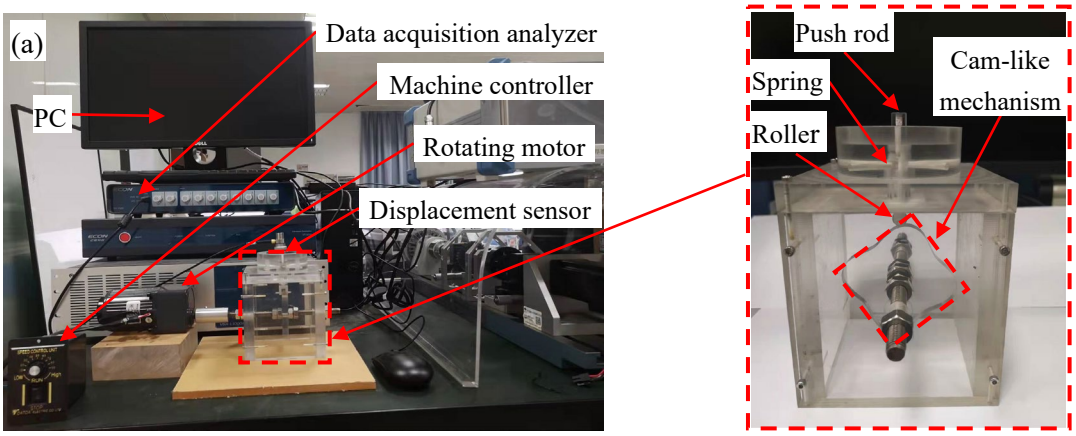

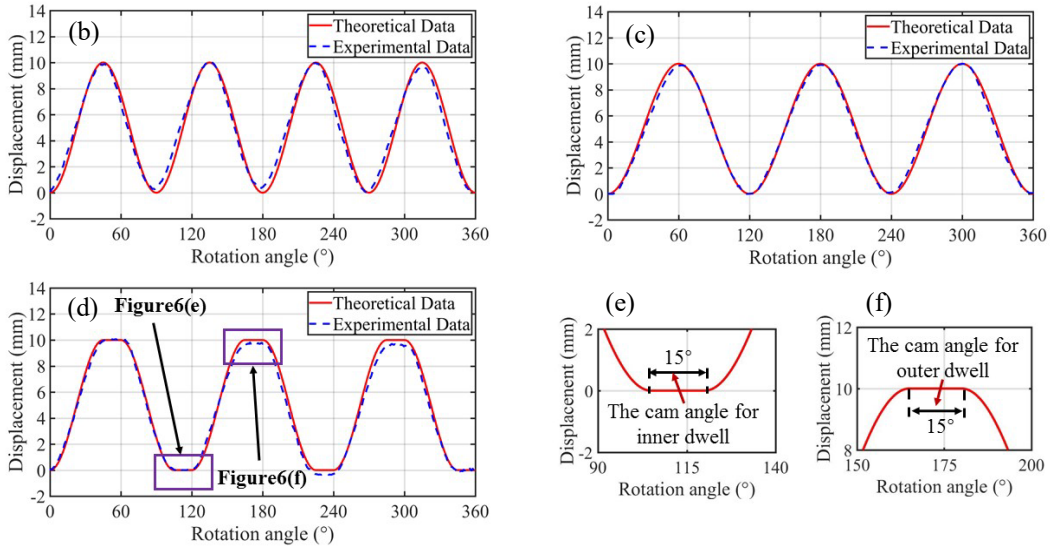

Fig. 7 (a) The experimental setup to verify the rotational-linear motion conversion rule. The tip displacement of the follower versus the rotating angles for (b) the four-protrusion cam with $H = 10$ mm, $r = 30$ mm and $\delta = \delta' = 45°$, (c) the three-protrusion cam with $H = 10$ mm, $r = 30$ mm and $\delta = \delta' = 60°$, (d) the three-protrusion cam with $H = 10$ mm, $r = 30$ mm, $\delta = \delta' = 45°$ and $\delta_s = \delta_s' = 15°$, and (e)(f) the zoomed figures of (d) to show the cam angles for inner dwell δ_s' and outer dwell δ_s, respectively.

The profile curve of the cam is the key factor that decides the rotational-linear motion conversion rule, which further decides the system dynamical and electrical responses. In this subsection, the rotational-linear motion conversion rule of a physical cam-like mechanism is studied. The cam-like mechanism models with three different cam types shown in Fig. 2 are manufactured, and the experimental setup involving a four-protrusion cam structure is shown in Fig. 7(a). It can be observed that a rotating motor with a controller is used to provide a precise rotational excitation for the cam, which further pushes the follower to move. The tip displacement of the follower is then measured by a displacement sensor (ECON, EV4200), and the data is collected by a data acquisition analyzer. The experimental results with different cam types are shown in Fig. 7(b)-(d), which present the tip displacement versus the rotation angle (between 0 and 360°). The theoretical curves were obtained through Eq. (2) and plotted in Fig. 7(b)-(d) for comparison. It can be observed that the experimental results match well with the theoretical ones with an error of approximately 3%. Such error may result from the machining error of the cam and follower, and the measurement error from the sensor. Thus, the rotational-linear motion conversion rule of the proposed cam-like mechanisms has been validated.

Moreover, Fig. 7(e) and (f) are two zoomed figures of Fig. 7(d), which show the displacement versus rotational angle of the three-protrusion cam structure with extra cam angles for outer dwell and inner dwell, respectively. It can be clearly observed that the design of the extra cam angles for outer dwell and inner dwell allows the follower to stay for a certain duration at both its furthest and closest positions relative to the cam. This indicates a potential advantage of the cam in providing an extra charging time and a discharging time, which in total account for 25% of the whole operating duration of the CDEG.

4.2 Fabrication of the pre-stretched DEM specimen

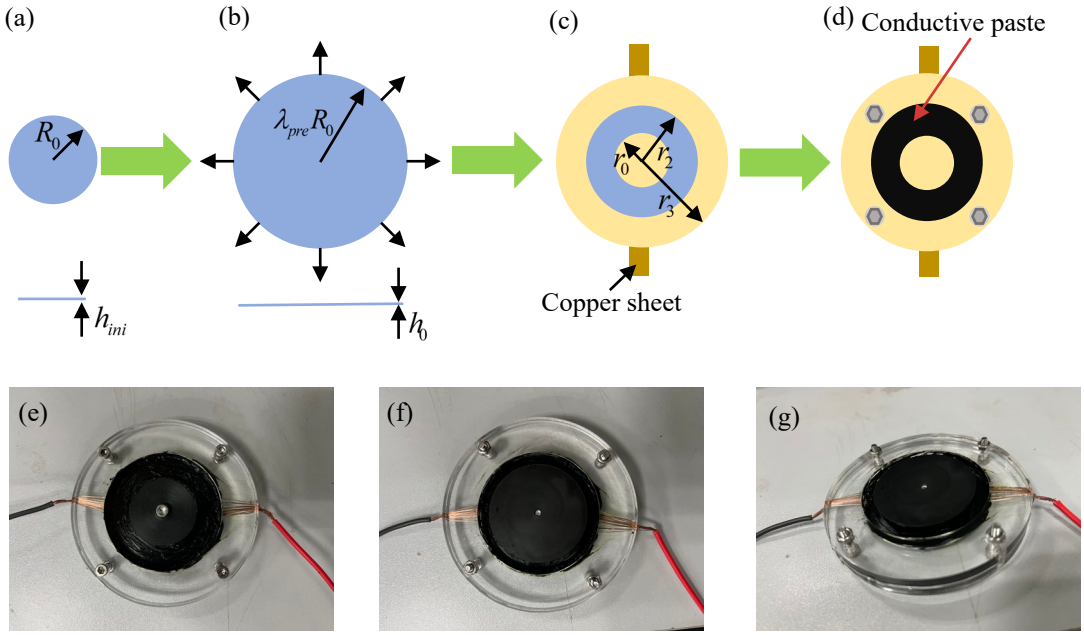

Fig. 8 The fabrication process of the pre-stretched DEM specimen: (a) The original DEM; (b) the pre-stretched DEM; (c) the pre-stretched DEM with annular-shaped clamps, disc-shaped clamp, mushroom-head clamp, and copper sheets; (d) the pre-stretched DEM coated with conductive paste; and (e)-(g) the finally obtained DEM specimen from different views.

The pre-stretched DEM specimens are further fabricated to assemble the CDEG. In this work, a round-type VHB 4910 membrane with the initial radius $R_0 = 40$ mm and the initial thickness $h_{ini} = 1$ mm is selected as the original specimen, as shown in Fig. 8(a). It should be noted that this type of membrane material is chosen as it is a type of commonly used dielectric elastomer, which can be obtained commercially and has been used in previous research work in Refs [-]. The original membrane is first stretched radially with a stretching ratio λ_{pre} to improve its stiffness and response speed ($\lambda_{pre} = 2$ in this experiment). After this, the thickness of the membrane is changed to $h_0 = h_{ini} / \lambda_{pre}^2$, as shown in Fig. 8(b). Next, two conductive copper sheets are placed on the upper and lower surfaces of the pre-stretched DEM, and two annular-shaped clamps with inner radius $r_2 = 25$ mm and outer radius $r_3 = 40$ mm are used to clamp the pre-stretched DEM. Furthermore, a disc-shaped clamp with radius $r_0 = 10$ mm and a mushroom-head clamp with the radiuses of upper and lower surfaces being $r_0 = 10$ mm and $r_1 = 15$ mm, respectively, are used to clamp the pre-stretched DEM. The obtained membrane is shown in Fig. 8(c). Finally, the exposed ring-shaped DEM is covered with conductive paste, as shown in Fig. 8(d). The experimental specimen of DEM shown in Fig. 8(e)-(g) is used for further experiments.

4.3 The capacitance measurement test

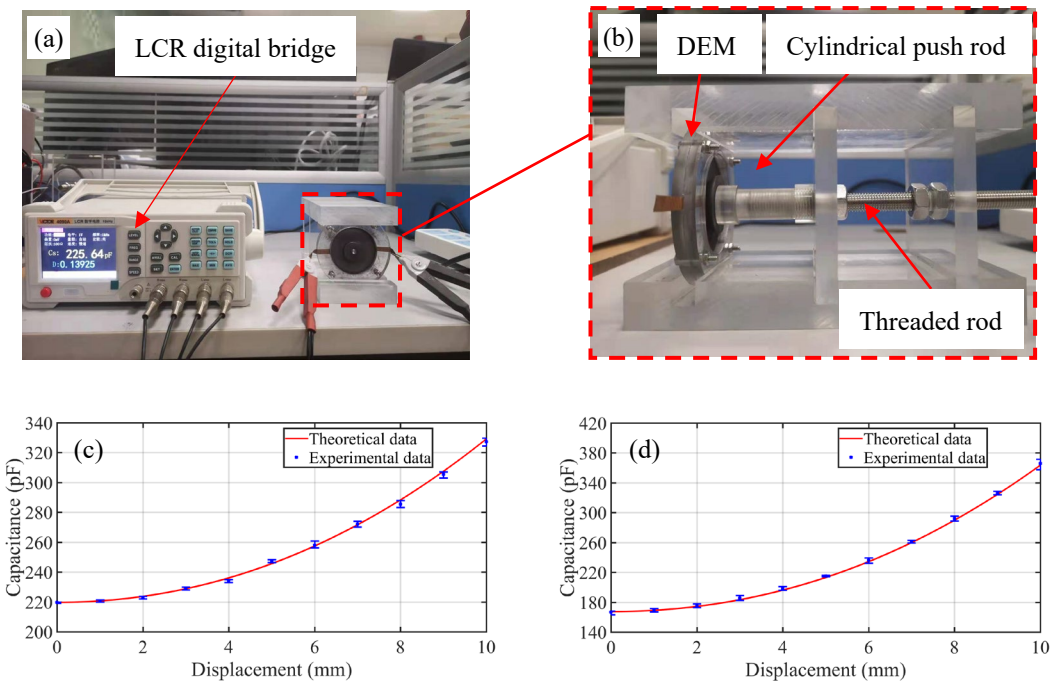

Fig. 9 (a) The experimental setup of the capacitance measurement test. (b) The zoomed view of the DEM stretching device. The capacitance of the DEM versus its deflections with (a) $r_0 = 10$ mm, $r_1 = 15$ mm and $r_2 = 25$ mm, and (d) $r_0 = 15$ mm, $r_1 = 20$ mm and $r_2 = 25$ mm.

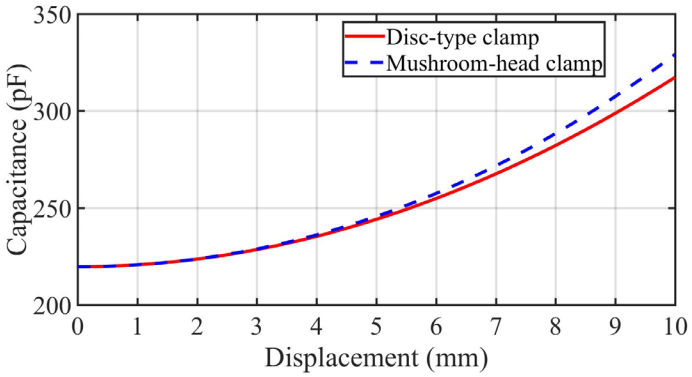

Fig. 10 Comparison of capacitance changes of DEMs with two different deformation modes.

It can be known from Eqs. (11) and (12) that the capacitance of the DEM under deformation is a key factor in generating the electrical output. In this work, the deformation of the DEM is quantified by its center deflection of the DEM (s), which equals to the tip displacement of the follower. In this subsection, a capacitance measurement test is conducted to verify the relationship between the capacitance and the tip displacement of the follower. The experimental setup for this is shown in Fig. 9(a)-(b). A pre-stretched DEM specimen is installed on a frame, and the mushroom-head clamp of the DEM is connected to a cylindrical push rod. The cylindrical push rod is further connected to a threaded rod with a radius of 5 mm. Thus, the tip displacement of the push rod can be adjusted by rotating the threaded rod, during which the DEM can be further deformed accordingly. An LCR digital bridge (VICTOR, VC4090A) is used to measure the capacitance of the DEM with varying deformation. In the tests, the capacitance data is measured when the tip displacement of the push rod increases from 1 to 10 mm, and the tests for each tip displacement are repeated by six times to reduce the measurement

error. The simulation and experimental results of the average capacitances of two DEMs with different dimensions against tip displacements are plotted in Fig. 9(c, d). It is noted that $\varepsilon_r = 3.7626$ is fitted to plot the simulated curves. One can see that the experimental results agree well with the theoretical ones, thus verifying the theoretical approach in calculating the capacitance of the deformed DEM.

To demonstrate the advantage of the mushroom-head clamp, the comparison experiment by replacing it with the disk-type clamp ($r_0 = 10$ mm and $r_2 = 25$ mm) is conducted. The resultant capacitance under different tip displacement is plotted in Fig. 10. One can see that the capacitance of the DEM with a mushroom-head clamp is larger than that with a disk-type clamp under the same tip displacement, thus enhancing the energy harvested by the system according to Eqs. (11) and (12).

4.4 The output voltage measurement experiment

Finally, a complete prototype of the proposed CDEG is manufactured, and an output voltage measurement experiment is performed to verify the theoretical analysis of the energy harvesting process as shown in Fig. 11(a). The experiment setup for this includes a CDEG prototype (Fig. 11(b)), a high-voltage power supply to provide the input voltage, a diode to prevent the inverse current, a rotating motor to drive the CDEG prototype, an energy harvesting circuit with a voltage divider (VDC) and a digital multimeter to measure the output voltage. In this setup, the voltage divider, which is composed of two resistors ($R_1 = 1$ GΩ and $R_2 = 1$ GΩ), is used to enable the output voltage to be measured by the digital multimeter. It is noted that all the designed cams shown in Fig. 2(b)-(d) are employed to assemble the CDEGs, and the corresponding CDEGs are marked as CDEG-A, CDEG-B, and CDEG-C, respectively.

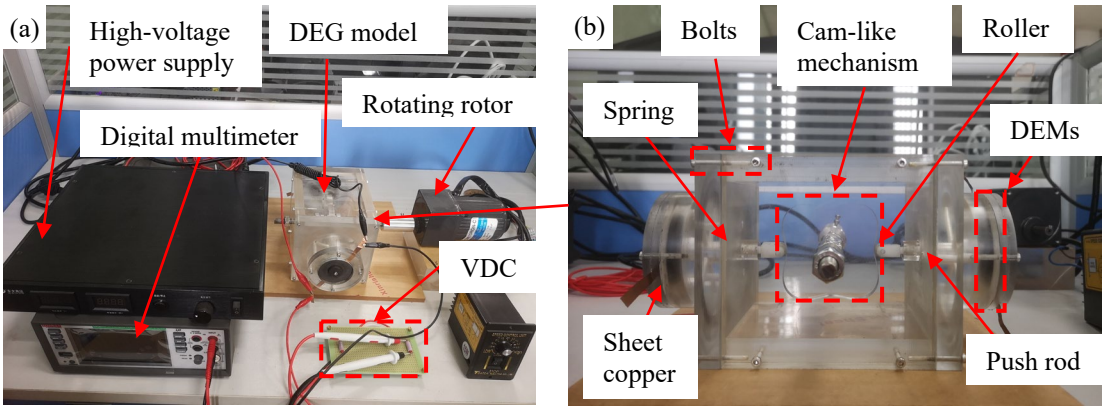

Fig. 11 (a) The output voltage measurement test system of the CDEG; (b) the prototype of a CDEG.

In the experiments, the initial states of both DEMs are set as Fig. 4(a). The rotation frequencyrotation frequency of the motor is set as 1 Hz, and the input voltage is set as 1000 V. When the CDEGs are under stable rotational excitations, the output voltages of one DEM in time domain are measured and recorded by the digital multimeter (Keithly, DAQ6510), as shown in Fig. 12. It can be seen from Fig. 12(a) there exist 16 output voltage peaks during 4 s, which corresponds to the ratio of the number of cam protrusions to that of one cam designed in the CDEG-A. Similarly, as the number of the cam protrusions of CDEG-B and CDEG-C is three, 12 or 13 obvious output voltage peaks appear during 4 s as shown in Fig. 12(b) and (c). The presented experimental results validate the effectiveness of the proposed CDEG in

rotational energy harvesting. It should be noted that in very limited cases the output voltage appears to be lower than the input voltage, which results from the micro vibration of the system due to the machining errors. Moreover, the average values of the output voltage peaks of the three types of CDEGs during a operational time interval are plotted in Fig. 12(d). It can be observed from Fig. 12(d) that in most cases the experimental voltage values are lower than the theoretical ones, which is inevitable due to the charge leakage and the energy dissipation of EH circuit [68].

Another important finding is that the average value of the output voltage peaks of CDEG-C is much higher than that of the CDEG-B, which is a bit higher than that of CDEG-A. This result can be explained from the charging and discharging time of each device. Compared CDEG-B with CDEG-A, the lifting/lowering angles of the three-protrusion cam are larger than those of the four-protrusion cam, thus providing more charging and discharging time for each DEM in one energy harvesting cycle. Hence, CDEG-B with a three-protrusion cam produced higher output voltage than that of CDEG-A with a four-protrusion cam under the same rotation frequency. Therefore, the CDEG-C, in which the cam profile is carefully designed to provide extra charging time and discharging time (see Fig. 7(d)), can produce the highest output voltage. These rsults evidently demonstrate the importance of sufficient charging and discharging time for the DEM in achieving the expected electrical output.

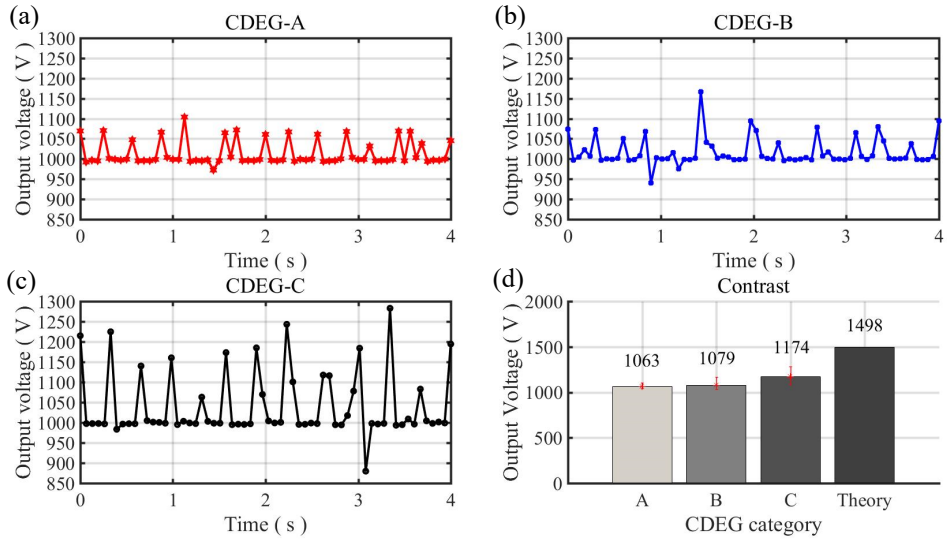

Fig. 12 The experimentally obtained output voltage in the time domain for (a) CDEG-A, (b) CDEG-B and (c) CDEG-C. (d) The experimental and theoretical average values of the output voltage peaks of different CDEGs.

5. Simulation and discussion

Table 1. Values of the parameters used in the numerical simulations.

Parameter	n	ϕ_{in}	λ_{pre}	H	r_0	r_1	r_2	ε_r
Value	1/6 Hz	1000 V	2	10 mm	10 mm	15 mm	25 mm	3.7626

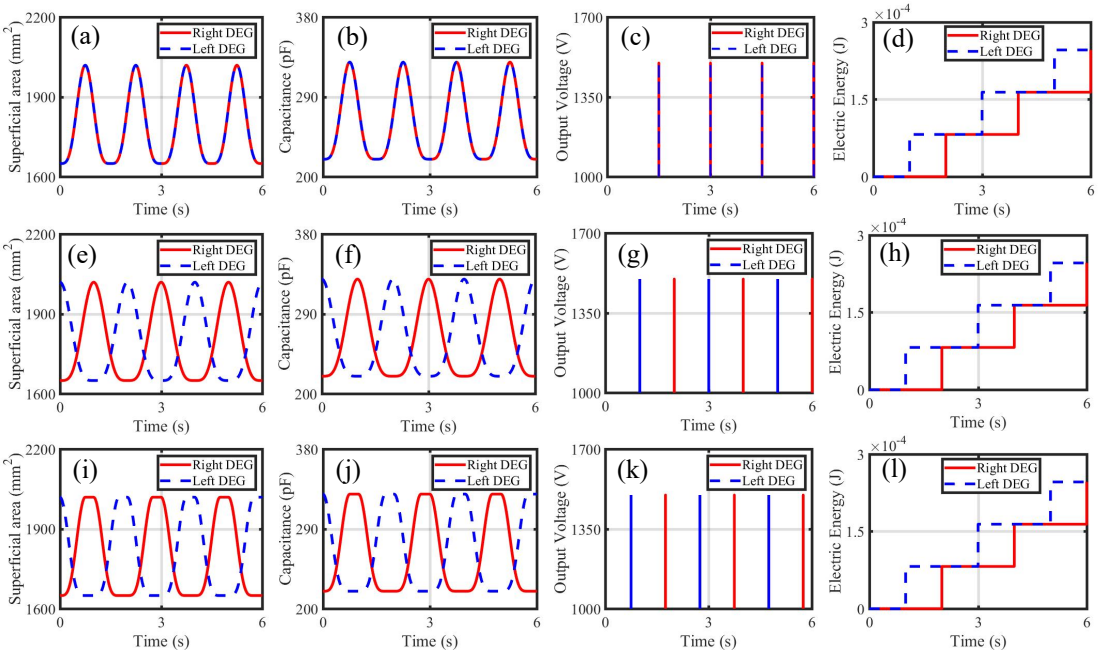

Fig. 13 (a)-(l) The effective area and the capacitance of each DEM, and the output voltage and the gained electrical energy in the time domain with (a)-(d), (e)-(h) and (i-l) respectively denoting those of CDEG-A, CDEG-B and CDEG-C, respectively.

The energy harvesting process of the proposed CDEG has been elaborated in Section 3 and verified in Section 4. With the validated theoretical model, the system dynamical and electrical outputs can be analyzed through numerical simulations, which are presented in this section. In the following simulations, the left and right rollers are assumed to contact the cam at positions of its minimum radius initially as shown in Fig. 4(a). The values of the parameters used in the simulations are presented in Table 1 unless otherwise stated. Specifically, the rotation frequency (n) is pre-set artificially. The input voltage (ϕ_{in}), the pre-stretched ratio (λ_{pre}) and other dimensional parameters (H, r_0, r_1 and r_2) are all set as the same as those in the experiments. The value of the relative dielectric constant of the DEM (ε_r) is identified from the experimental results of capacitance in Fig. 9. Thus, the system responses of CDEG-A, CDEG-B, and CDEG-C can be obtained numerically, as shown in Fig. 13. It can be observed that when excited by a rotation with a constant rotation frequency, the effective area and capacitance of both DEMs vary periodically. The output voltage peaks can be produced when the capacitance of DEMs drops from the highest value to the lowest one. At each energy harvesting cycle, the electrical energy harvested can be calculated, and the output power during a given time interval can be further obtained, which are 0.1094 mW, 0.0820 mW and 0.0820 mW for CDEG-A, CDEG-B, and CDEG-C, respectively.

It can be known from our previous analyses that the system EH performance, which can be evaluated by the output power, is affected by the excitation and dimensional parameters. According to Eq. (14), it is obvious that there is a linear correlation between the output power P_{sys} and the rotation frequency n, and a linear correlation between P_{sys} and the number of cam protrusions N. Hence, the output power can be enhanced by increasing the values of n and N (which should be a positive integer). However, a higher rotation frequency will shorten the charging and discharging time of the DEMs at each energy harvesting cycle, thus reducing

the energy harvested at each cycle. Therefore, there exists an optimal rotation frequency for a CDEG, which can be obtained through experiment. In addition, increasing the number of the cam protrusions will increase the size of the cam-like mechanism, leading to a significant drop of the energy density. Therefore, the number of the cam protrusions is not a desirable parameter for the optimization of EH performance.

In the following of this section, the influences of several important parameters, including the system dimensional parameters, the pre-stretched ratio of the DEMs and the input voltage on the system EH performance are studied and analyzed comprehensively. Following this, the system parameters are optimized through the Genetic algorithm. It is noted that the subsequent simulations use CDEG-A with a four-protrusion cam structure as representative, and the influence mechanisms of system parameters are also applicable for other CDEGs.

5.1 Influences of the system dimensional parameters

It can be seen from Eq. (14) that when the rotation frequency and the number of cam protrusions are given in advance, the system output power is decided by the generated electrical energy of each energy harvesting cycle, which is in fact decided by the system dimensional parameters, as shown in Eq. (12). Hence, the system dimensional parameters, such as the lifting distance of the cam (H), the radius of the disc-shaped clamp (r_0), the radius of the lower surface of the mushroom-head clamp (r_1) and the inner radius of the annular clamp (r_2), have significant effects on the system EH performance. The numerical simulation approach is adopted in this subsection to reveal this.

In the following simulation, it is ensured that the DEMs will not be damaged at their largest deformations. This can be guaranteed when the ultimate stretch ratio λ_u of the DEMs at their largest deformation does not exceed the limited stretched ratio $\lambda_{\lim}$ of the employed DE material, i.e., $\lambda_u \le \lambda_{\lim}$. For the VHB 4910 membrane used in this work, the value of $\lambda_{\lim}$ is approximately 5.5 [69]. In this work, the DEM is firstly pre-stretched and then stretched during the deformation, therefore $\lambda_u = \lambda_{pre}\lambda_{def}$. Here, $\lambda_{def} = \sqrt{A_{\max} / (\pi r_2^2 - \pi r_0^2)} = \sqrt{h_0 / h_{\min}}$ indicates the largest stretch ratio of the DEM when it is under the largest out-of-plane deformation. It is apparent that the value of λ_{def} is decided by the system dimensional parameters. Thus, the system dimensional parameters should be carefully selected to guarantee the following condition:

$$\lambda_{def} = \lambda_u / \lambda_{pre} \le \lambda_{\lim} / \lambda_{pre} \tag{15}$$

With Inequality (15) satisfied, the relationships of the output voltage and the output power versus H, r_0, r_1 and r_2 are plotted in Fig. 14(a)-(d), respectively. Firstly, it can be observed from Fig. 14 (a) that when the lifting distance of the cam (H) increases from 5 mm to 20 mm, the output voltage of each energy harvesting cycle and the system output power increase correspondingly. This is due to the fact that a larger H results in a larger effective area $A_{\max}$ of the DEM at its largest deformation, thus producing a higher output voltage and a larger output power with other parameters unchanged based on Eq. (11)-(13). Secondly, Fig. 14(b) shows the influence of the radius of the disc-shaped clamp (r_0). Here, the value range of r_0 is set as $5 \le r_0 \le 20$ mm due to the limitation from Eq. (15). It can be observed that r_0 also has a

positive impact on the system EH performance. Thirdly, the output voltage and power versus the radius of the lower surface of the mushroom-head clamp (r_1) are plotted in Fig. 14(c). The value of r_1 is set between 10 mm and 25 mm with Eq. (15) satisfied. It can be observed that the output voltage and power both increase with the increase of r_1, indicating that r_1 has a positive effect on the EH performance of the system. However, compared with the effects of H and r_0 on the output power, this effect is relatively weaker. This is due to the fact that the increase of r_1 has less effect on the total area of the DEM (A) than that of H and r_0. This can be derived from Eq. (3). According to Eqs. (11)-(12), it can be seen that both the output voltage and power have a positive relationship with the maximum area of the DEM. Finally, the curves of the output voltage and power versus the inner radius of the annular clamp (r_2) are plotted in Fig. 14(d). The value of r_2 is set between 20 mm and 35 mm due to the limitation from Eq. (15). Both curves present a decreasing trend as the value of r_2 increases.

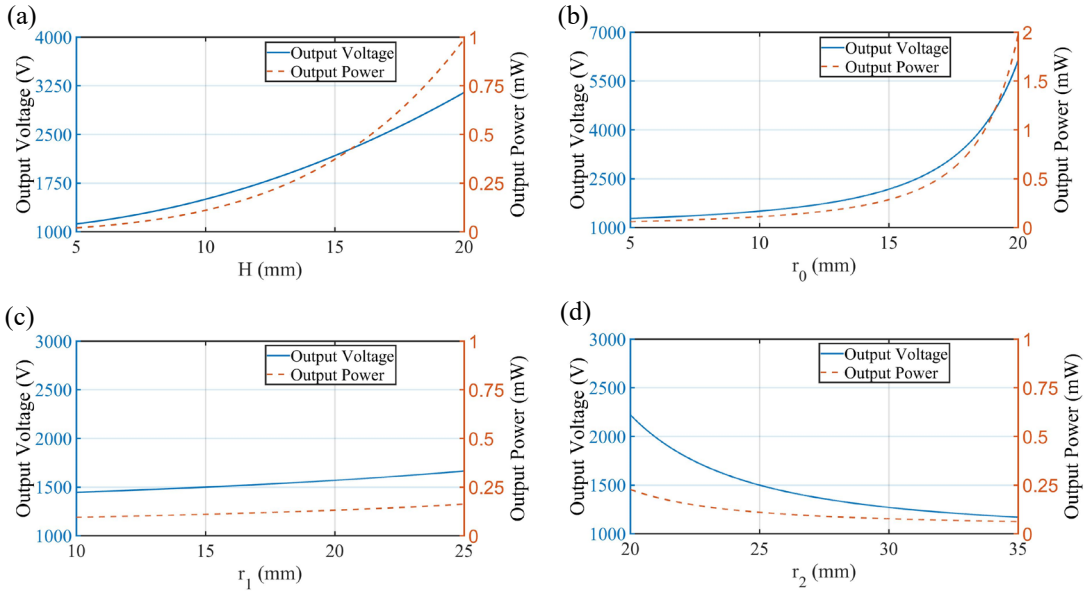

Fig. 14 The output voltage and output power of the CDEG-A versus (a) H with $r_0 = 10$ mm, $r_1 = 15$ mm and $r_2 = 25$ mm, (b) r_0 with $H = 10$ mm, $r_1 = 15$ mm and $r_2 = 25$ mm, (c) r_1 with $H = 10$ mm, $r_0 = 10$ mm and $r_2 = 25$ mm, and (d) r_2 with $H = 10$ mm, $r_0 = 10$ mm and $r_1 = 15$ mm.

In addition, the relationships of the mass energy density (MED) and the volume energy density(VED) (indicating the output power over unit mass and unit volume, respectively) versus H, r_0, r_1 and r_2 are plotted in Fig. 15(a)-(d). The overall regulations of curves are consistent with the those shown in Fig. 14(a)-(d).

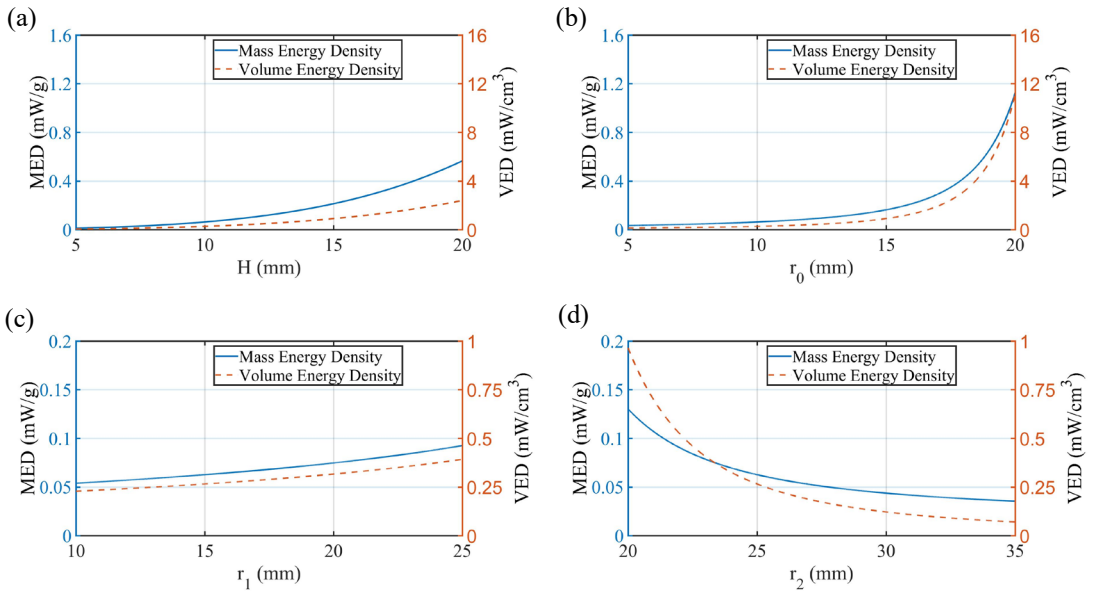

Fig. 15 The MED and VED of the CDEG-A versus (a) H with $r_0 = 10$ mm, $r_1 = 15$ mm and $r_2 = 25$ mm, (b) r_0 with $H = 10$ mm, $r_1 = 15$ mm and $r_2 = 25$ mm, (c) r_1 with $H = 10$ mm, $r_0 = 10$ mm and $r_2 = 25$ mm, and (d) r_2 with $H = 10$ mm, $r_0 = 10$ mm and $r_1 = 15$ mm.

It can be concluded from Fig. 14 that the EH performance of the CDEG can be enhanced by increasing the values of H, r_0, r_1 or decreasing the value of r_2. However, as we mention previously, the requirements of Inequality (15) and $r_0 \le r_1 \le r_2$ must be satisfied, indicating that these four dimensional parameters have a coupling effect on the system EH performance and cannot be adjusted separately. Hence, their combined influence on the system EH performance should be further studied. It is noted that the value of H is not further adjusted since the cam design is assumed to be fixed. In the following simulations, $r_0 + 5 \le r_1 \le r_2$ is satisfied to guarantee that the radius of the arc side of the mushroom-head clamps ($R = r_1 - r_0$) is larger than 5 mm. Firstly, the system output voltage and generated power versus different sets of r_0 and r_1 with $r_2 = 25$ mm are plotted in Fig. 16(a) and (b), respectively. A clear observation is that both r_0 and r_1 have a positive effect on the system EH performance, and the maximum output voltage and the maximum output power are respectively 2170.0 V and 0.2835 mW at the largest values of both r_0 and r_1. Next, by setting $r_1 = 20$ mm constantly, the combined effect of r_0 and r_2 are presented in Fig. 16(c) and (d). In the premise of $r_0 + 5 \le r_1 \le r_2$, the maximum output voltage (6434.1 V) and maximum power (1.7098 mW) appear when the r_0 is largest and the r_1 is smallest. Finally, the value of r_0 is set as 10 mm, and the system output voltage and power versus different sets of r_1 and r_2 are respectively plotted in Fig. 16(e) and (f). It can be known from the figure that to achieve a better EH performance, r_1 should be increased whereas r_2 should be decreased with $r_1 \le r_2$ satisfied. The simulation results show that the maximum voltage (7053.1 V) and maximum power (1.4923 mW) are obtained when the value of r_2 is minimum and $r_1 = r_2$, which means that r_2 has a stronger effect on the system EH performance than r_1.

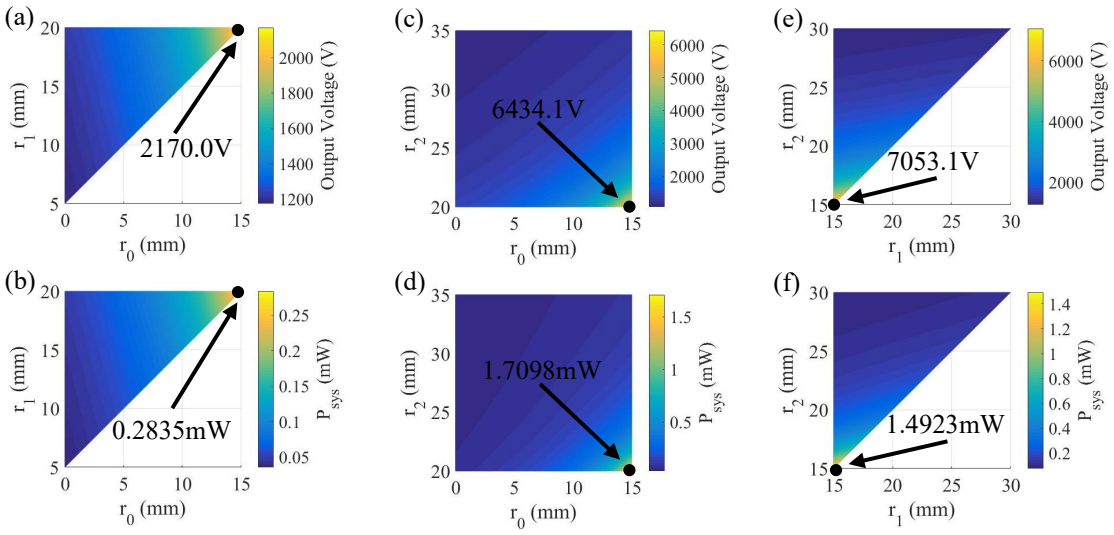

Fig. 16 The output voltage and output power under different sets of: (a)(b) r_0 and r_1, (c)(d) r_0 and r_2, (e)(f) r_1 and r_2.

In summary, the EH performance of the system can be enhanced by increasing the values of H, r_0, r_1 and decreasing the value of r_2. However, their combination is limited by the stretched ratio of the DE materials at the largest deformation of the DEM, which is presented by Inequality (15). It can be concluded from Fig. 16 that when r_2 is fixed, the larger r_0 and r_1 have a positive effect on the EH performance of CDEG. When r_1 is fixed, r_0 should be as large as possible whereas r_2 should be as small as possible. When r_0 is constant, the optimal EH performance will appear at the condition when r_1 becomes as large as r_2.

5.2 Influences of the pre-stretched ratio and the input voltage

The values of the pre-stretch ration λ_{pre} and the input voltage ϕ_{in} also affect the system EH performance. Considering that $\lambda_u = \lambda_{pre}\lambda_{def} \le \lambda_{\lim}$, when the system dimensional parameters are fixed, the largest value of λ_{pre} can be calculated as $\lambda_{\lim} / \lambda_{def}$. For example, when other parameters are set as shown in Table 1, the upper limit of λ_{pre} is 2.5, which means that $1 \le \lambda_{pre} \le 2.5$ should be satisfied. Under this constraint, the influence of λ_{pre} on the system EH performance is presented in Fig. 17(a). It can be seen that increasing the value of λ_{pre} poses little influences on the output voltage, which can be known from Eq. (11) as well. However, increasing λ_{pre} will result in the higher energy harvested in one energy harvesting cycle due to a smaller initial thickness h_0 according to Eq. (12), thus producing the higher output power as shown in Fig. 17(a). Therefore, increasing the pre-stretched ratio can not only improve the stiffness and response speed of the DEM but also enhance the system EH performance.

As for the influences of the input voltage ϕ_{in}, it can be known from Eq. (11)-(14) that it has a linear correlation with the output voltage, and more importantly, the output power has a squared correlation with ϕ_{in}.This can also be observed from the curve types shown in Fig.

17(b). Therefore, the input voltage is a feasible parameter to enhance the system EH performance. However, it should be noted that there exists a breakdown voltage for the DE material [69], leading to the fact that the input voltage cannot be increased infinitely.

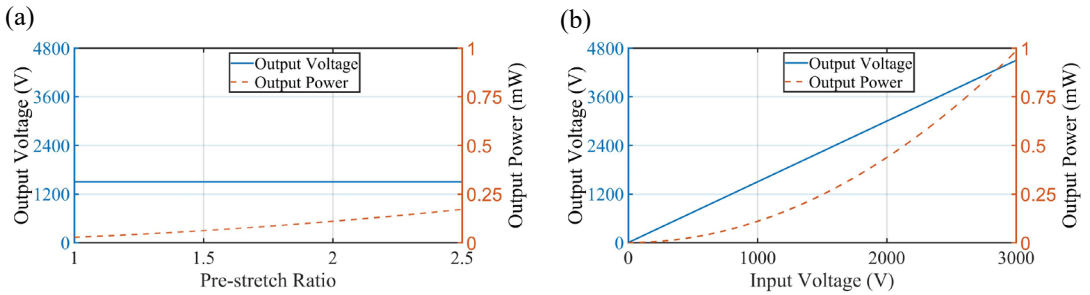

Fig. 17 The output voltage and output power of the CDEG versus (a) pre-stretch ratio, (b) input voltage.

Moreover, the relationships of the MED and the VED against the pre-stretch ration λ_{pre} and the input voltage ϕ_{in} are plotted in Fig. 18(a)-(d), respectively. It can be observed that the MED and VEH both increase with the increasing H, r_0 and r_1 whereas decrease with the increasing r_2.

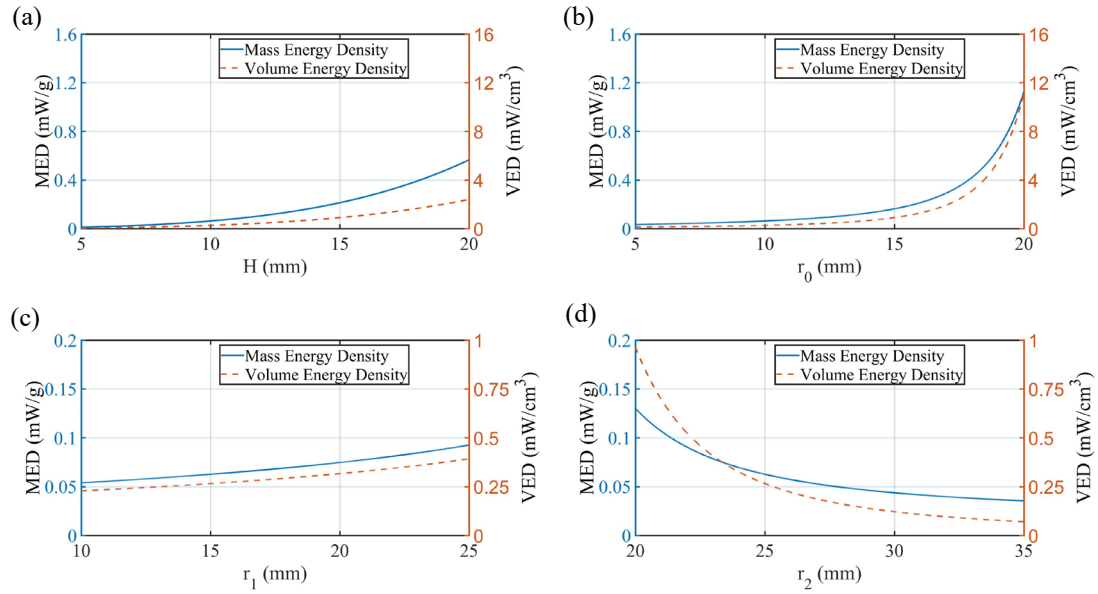

Fig. 18 The MED and VED of the CDEG versus (a) pre-stretch ratio, (b) input voltage.

5.3 Optimization of the system parameters based on Genetic algorithm

From the above analysis, it can be known that the system parameters, especially the dimensional parameters, have a combined and relatively complicated influence on the EH performance of the proposed CDEG. In this subsection, the multi-parameter Genetic optimization algorithm [70], is further adopted to derive the optimal parameter sets with respect to the EH performance. In the optimization, the values of n, ϕ_{in} and H are set as shown in Table 1, and the output power is set to be the optimization objective. The rotation frequency is set as 0.17 Hz, and the values of r_0, r_1, r_2 and λ_{pre} are optimized with the inequalities of $5 \le r_0 + 5 \le r_1 \le r_2 \le 25$ and $\lambda_u = \lambda_{pre}\lambda_{def} \le \lambda_{\lim}$. The optimization results show that the

maximum output power of 2.8910 mW can be achieved with the optimal parameters of $r_0 = 17.8988$ mm, $r_1 = 22.9012$ mm, $r_2 = 22.9020$ mm and $\lambda_{pre} = 2.5$.

For comparison, the maximum output power P_m and the normalized power NP of some typical rotational energy harvesters obtained from their simulation results are presented in Table 2. Note that harvesters based on different transduction methods have been selected to compare. With the goal to estimate their energy conversion capacity at ultra-low rotational frequencies, the normalized output power NP is defined by taking the rotational frequency f into account as follows:

$$NP = \frac{P_m}{f^2} \tag{16}$$

It can be seen that the system output power of the proposed CDEG has the highest output power compared with others. Furthermore, its superior energy conversion capacity at ultra-low rotational frequencies is reflected in the highest normalized power as well. The comparison results demonstrate the advantages of the proposed CDEG in rotational energy harvesting. Overall, the proposed CDEG is potentially used in ultra-low-frequency (< 1 Hz) applications, for instance, wind turbines and ocean wave motions.

Table 2. Comparison between the EH performance of the proposed CDEG and typical rotational energy harvesters in literature.

Reference	Energy conversion mechanism	Rotation frequency (Hz)	Maximal output power (mW)	Normalized power (mW/Hz^2)
Zhang *et al*. [71]	Piezoelectric	5-9.2	0.0810	0.0009-0.0032
Mei *et al*. [72]	Piezoelectric	6	0.4900	0.0136
Xie *et al*. [73]	Piezoelectric	12	0.0650	0.0005
Malaji *et al*. [74]	Electromagnetic	2.5	0.2500	0.0400
Feng *et al*. [75]	Electromagnetic	65	0.0203	4.8×10^{-6}
Zhang *et al*. [62]	Electrostatic	0.17	0.2753	9.5260
The proposed CDEG	Electrostatic	0.17	2.8910	100.0346

6. Conclusions

In order to take advantage of the dielectric elastomer (DE) materials to harvest energy from ubiquitous rotational environments, a novel cam-like dielectric elastomer generator (CDEG) for high-performance rotational energy harvesting is proposed and studied in this paper. In the CDEG, the improved mushroom-head type clamp is designed to form a type of advanced conical DEMs, and the multi-protrusion cams with different profile curves are designed to convert any rotational motion into the linear reciprocating motion. The working mechanism of the CDEG is analyzed theoretically to derive the system dynamical and electrical output. The theoretical analyses are verified experimentally by measuring the rotational-linear motion conversion rule of the cam-like mechanism, the capacitance of the DEM under deformation, and the output voltage of the system under rotational excitations. With the validated theoretical model, the numerical simulations are further conducted to reveal the influences of the system dimensional parameters, pre-stretched ratio, and input voltage on the system energy output,

thus providing guidelines for parameter adjustments to improve the system performance. The Genetic algorithm is further adopted to optimize the system parameters and obtain the corresponding optimal EH performance of the proposed CDEG, which is superior than other typical rotational energy harvesters in literature. The simulation and experimental results show that the adequate charging time and discharging time with the proposed design are beneficial to the EH performance. The parameter adjustment and optimization approaches presented in this work are valuable for the practical design of the CDEG on demand.

Acknowledgments

This work was supported by the National Natural Science Foundation of China (Grant Nos. 52205114, 51905349, U2013603), Guangdong Basic and Applied Basic Research Foundation (Grant Nos. 2022A1515010126, 2020A1515011509), Natural Science Foundation of Shenzhen University (Grant No. 860-000002110264) and Shenzhen Natural Science Fund (the Stable Support Plan Program 20220809181431001).

References

1 Fan K., Hao J., Tan Q., et al. A monostable hybrid energy harvester for capturing energy from low-frequency excitations. Journal of Intelligent Material Systems and Structures, 2019, 30(18-19): 2716-2732.

2 Xue F., Chen L., Li C., et al. A static-dynamic energy harvester for a self-powered ocean environment monitoring application. Science China Technological Sciences, 2022, 65(4): 893-902.

3 Zhang B., Liu H., Zhou S., et al. A review of nonlinear piezoelectric energy harvesting interface circuits in discrete components. Applied Mathematics and Mechanics, 2022, 43(7): 1001-1026.

4 Li X., Tang H., Hu G., et al. ViPSN-Pluck: a transient-motion-powered motion detector. IEEE Internet of Things Journal, 2021, 9(5): 3372-3382.

5 Lau D., Song N., Hall C., et al. Hybrid solar energy harvesting and storage devices: The promises and challenges. Materials Today Energy, 2019, 13: 22-44.

6 Hu G., Wang J., Tang L. A comb-like beam based piezoelectric system for galloping energy harvesting. Mechanical Systems and Signal Processing, 2021, 150: 107301.

7 Gu S., Wang J., Hu G., et al. Prediction of wind-induced vibrations of twin circular cylinders based on machine learning. Ocean Engineering, 2021, 239: 109868.

8 Papini G. P. R., Moretti G., Vertechy R., et al. Control of an oscillating water column wave energy converter based on dielectric elastomer generator. Nonlinear Dynamics, 2018, 92(2): 181-202.

9 Lai Z., Xu J., Bowen C. R., et al. Self-powered and self-sensing devices based on human motion. Joule, 2022, 6: 1501–1565.

10 Ma X., Li H., Zhou S., et al. Characterizing nonlinear characteristics of asymmetric tristable energy harvesters. Mechanical Systems and Signal Processing, 2022, 168.

11 Zhang Y., Lu Y., Chen L. Energy harvesting via nonlinear energy sink for whole-spacecraft. Science China Technological Sciences, 2019, 62(9): 1483-1491.

12 Yan B., Yu N., Ma H., et al. A theory for bistable vibration isolators. Mechanical Systems and Signal Processing, 2022, 167: 108507.

13 Zhao L., Zou H., Gao Q., et al. Design, modeling and experimental investigation of a

magnetically modulated rotational energy harvester for low frequency and irregular vibration. Science China Technological Sciences, 2020, 63: 2051-2062.

14 Fu H., Yeatman E. M. Rotational energy harvesting using bi-stability and frequency up-conversion for low-power sensing applications: Theoretical modelling and experimental validation. Mechanical Systems and Signal Processing, 2019, 125: 229-244.

15 Fang S., Wang S., Zhou S., et al. Analytical and experimental investigation of the centrifugal softening and stiffening effects in rotational energy harvesting. Journal of Sound and Vibration, 2020, 488: 115643.

16 Bao B., Wang Q. Bladeless rotational piezoelectric energy harvester for hydroelectric applications of ultra-low and wide-range flow rates. Energy Conversion and Management, 2021, 227: 113619.

17 Cai M., Liao W.-H. Enhanced electromagnetic wrist-worn energy harvester using repulsive magnetic spring. Mechanical Systems and Signal Processing, 2021, 150: 107251.

18 Lu Z., Zhang F., Fu H., et al. Rotational nonlinear double-beam energy harvesting. Smart Materials and Structures, 2021, 31(2): 025020.

19 Fu H., Mei X., Yurchenko D., et al. Rotational energy harvesting for self-powered sensing. Joule, 2021, 5(5): 1074-1118.

20 Zhang Y., Cao J., Zhu H., et al. Design, modeling and experimental verification of circular Halbach electromagnetic energy harvesting from bearing motion. Energy Conversion and Management, 2019, 180: 811-821.

21 Zaouali E., Najar F., Kacem N., et al. Pendulum-based embedded energy harvester for rotating systems. Mechanical Systems and Signal Processing, 2022, 180: 109415.

22 Zhang Y., Wang W., Xie J., et al. Enhanced variable reluctance energy harvesting for self-powered monitoring. Applied Energy, 2022, 321: 119402.

23 Wang Y., Yang Z., Li P., et al. Energy harvesting for jet engine monitoring. Nano Energy, 2020, 75: 104853.

24 Gao F., Liu G., Chung B. L.-H., et al. Macro fiber composite-based energy harvester for human knee. Applied Physics Letters, 2019, 115(3): 033901.

25 Pang Y., Cao Y., Derakhshani M., et al. Hybrid energy-harvesting systems based on triboelectric nanogenerators. Matter, 2021, 4(1): 116-143.

26 Zhao C., Zhang Q., Zhang W., et al. Hybrid piezo/triboelectric nanogenerator for highly efficient and stable rotation energy harvesting. Nano Energy, 2019, 57: 440-449.

27 Bai Y., Jantunen H., Juuti J. Energy Harvesting Research: The Road from Single Source to Multisource. Advanced Materials, 2018, 30(34).

28 Miao G., Fang S., Wang S., et al. A low-frequency rotational electromagnetic energy harvester using a magnetic plucking mechanism. Applied Energy, 2022, 305.

29 Tan Y., Dong Y.,Wang X. Review of MEMS Electromagnetic Vibration Energy Harvester. Journal of Microelectromechanical Systems, 2017, 26(1): 1-16.

30 Yang K., Tong W. H., Lin L. Q., et al. Active vibration isolation performance of the bistable nonlinear electromagnetic actuator with the elastic boundary. Journal of Sound and Vibration, 2022, 520: 116588.

31 O'Donnell T., Saha C., Beeby S. P., et al. Scaling Effects for Electromagnetic Vibrational Power Generators. Microsystem Technologies, 2007, 13(11): 1637-1645.

32 Bai Y., Tofel P., Hadas Z., et al. Investigation of a cantilever structured piezoelectric energy

harvester used for wearable devices with random vibration input. Mechanical Systems and Signal Processing, 2018, 106: 303-318.

33 Wang S., Liao W., Zhang Z., et al. Development of a novel non-contact piezoelectric wind energy harvester excited by vortex-induced vibration. Energy Conversion and Management, 2021, 235.

34 Fang S., Zhou S., Yurchenko D., et al. Multistability phenomenon in signal processing, energy harvesting, composite structures, and metamaterials: A review. Mechanical Systems and Signal Processing, 2022, 166: 108419.

35 Wang J., Tang L., Zhao L., et al. Efficiency investigation on energy harvesting from airflows in HVAC system based on galloping of isosceles triangle sectioned bluff bodies. Energy, 2019, 172: 1066-1078.

36 Kang-Kang W., Xian-Bin L., Yu Z. Stochastic resonance and stability for a stochastic metapopulation system subjected to non-Gaussian noise and multiplicative periodic signal. Physica Scripta, 2015, 90(8): 085002.

37 Wang S., Lin L., Wang Z. L. Triboelectric nanogenerators as self-powered active sensors. Nano Energy, 2015, 11: 436-462.

38 Crovetto A., Wang F.,Hansen O. Modeling and Optimization of an Electrostatic Energy Harvesting Device. Journal of Microelectromechanical Systems, 2014, 23(5): 1141-1155.

39 Khan F. U., Qadir M. U. State-of-the-art in vibration-based electrostatic energy harvesting. Journal of Micromechanics and Microengineering, 2016, 26(10).

40 Kaltseis R., Keplinger C., Koh S. J. A., et al. Natural rubber for sustainable high-power electrical energy generation. Rsc Advances, 2014, 4(53): 27905-27913.

41 Boisseau S., Despesse G., Sylvestre A. Optimization of an electret-based energy harvester. Smart Materials and Structures, 2010, 19(7).

42 Chiu Y., Lee Y.-C. Flat and robust out-of-plane vibrational electret energy harvester. Journal of Micromechanics and Microengineering, 2013, 23(1).

43 Morrissey T. G., Mitchell S. K., Jaros A. T., et al. Mechanical-to-Electrical Energy Conversion with Variable Electric Double Layers. Energy Technology, 2019, 7(4).

44 Zhang C. L., Lai Z. H., Zhang G. Q., et al. Energy harvesting from a dynamic vibro-impact dielectric elastomer generator subjected to rotational excitations. Nonlinear Dynamics, 2020, 102(3): 1271-1284.

45 Pelrine R., Kornbluh R., Eckerle J., et al. *Dielectric elastomers: Generator mode fundamentals and applications*. in *Smart Structures and Materials 2001 Conference*. 2001. Newport Beach, Ca.

46 Cao J., Lu G., Shiju E., et al. Electrostatic model of dielectric elastomer generator based on finite element. Scientific Reports, 2021, 11(1).

47 Di K., Bao K., Chen H., et al. Dielectric Elastomer Generator for Electromechanical Energy Conversion: A Mini Review. Sustainability, 2021, 13(17).

48 Moretti G., Fontana M., Vertechy R. Parallelogram-shaped dielectric elastomer generators: Analytical model and experimental validation. Journal of Intelligent Material Systems and Structures, 2015, 26(6): 740-751.

49 Righi M., Moretti G., Forehand D., et al. A broadbanded pressure differential wave energy converter based on dielectric elastomer generators. Nonlinear Dynamics, 2021, 105(4): 2861-2876.

50 Moretti G., Scialo A., Malara G., et al. Hardware-in-the-loop simulation of wave energy converters based on dielectric elastomer generators. Meccanica, 2021, 56(5): 1223-1237.

51 McKay T., O'Brien B., Calius E., et al. An integrated, self-priming dielectric elastomer generator. Applied Physics Letters, 2010, 97(6).

52 Kornbluh R., Pelrine R., Pei Q. B., et al. *Electroelastomers: Applications of dielectric elastomer transducers for actuation, generation and smart structures*. in *Smart Structures and Materials 2002 Conference*. 2002. San Diego, Ca.

53 Yurchenko D., Lai Z. H., Thomson G., et al. Parametric study of a novel vibro-impact energy harvesting system with dielectric elastomer. Applied Energy, 2017, 208: 456-470.

54 Yurchenko D., Val D. V., Lai Z. H., et al. Energy harvesting from a DE-based dynamic vibro-impact system. Smart Materials and Structures, 2017, 26(10).

55 Lai Z., Wang S., Zhu L., et al. A hybrid piezo-dielectric wind energy harvester for high-performance vortex-induced vibration energy harvesting. Mechanical Systems and Signal Processing, 2021, 150.

56 Lai Z., Wang J., Zhang C., et al. Harvest wind energy from a vibro-impact DEG embedded into a bluff body. Energy Conversion and Management, 2019, 199.

57 Jean-Mistral C., Basrour S.,Chaillout J.-J. *Dielectric polymer: scavenging energy from human motion*. in *Conference on Electroactive Polymer Actuators and Devices (EAPAD 2008)*. 2008. San Diego, CA.

58 Armbruster P., Oster Y., Vogt M., et al. Design of a mechanism for converting the energy of knee motions by using electroactive polymers. Biomedical Engineering-Biomedizinische Technik, 2017, 62(6): 643-652.

59 Fan P., Zhu L., Zhu Z., et al. Predicting energy harvesting performance of a random nonlinear dielectric elastomer pendulum. Applied Energy, 2021, 289.

60 Vu-Cong T., Jean-Mistral C., Sylvestre A. Electrets substituting external bias voltage in dielectric elastomer generators: application to human motion. Smart Materials and Structures, 2013, 22(2).

61 Zhang C. L., Lai Z. H., Li M. Q., et al. Wind energy harvesting from a conventional turbine structure with an embedded vibro-impact dielectric elastomer generator. Journal of Sound and Vibration, 2020, 487.

62 Zhang J., Lai Z., Rao X., et al. Harvest rotational energy from a novel dielectric elastomer generator with crank-connecting rod mechanisms. Smart Materials and Structures, 2020, 29(6).

63 Bortot E., Gei M. Harvesting energy with load-driven dielectric elastomer annular membranes deforming out-of-plane. Extreme Mechanics Letters, 2015, 5: 62-73.

64 Jiang Y., Liu S., Zhong M., et al. Optimizing energy harvesting performance of cone dielectric elastomer generator based on VHB elastomer. Nano Energy, 2020, 71.

65 Guo R. Checking computations pressure angle for symmetrical translation cam. Journal of Machine Design, 1985(01): 55-58.

66 Mckay T. G., Rosset S., Anderson I. A., et al. Dielectric elastomer generators that stack up. Smart Materials & Structures, 2015, 24(1): 015014.

67 Moretti G., Rosset S., Vertechy R., et al. A Review of Dielectric Elastomer Generator Systems. Advanced Intelligent Systems, 2020, 2(10).

68 Zhang C. L., Lai Z. H., Rao X. X., et al. Energy harvesting from a novel contact-type dielectric elastomer generator. Energy Conversion and Management, 2020, 205.

69 Koh S., Keplinger C., Li T., et al. Dielectric Elastomer Generators: How Much Energy Can Be Converted? IEEE/ASME Transactions on Mechatronics, 2011, 16(1): 33-41.

70 Chahar V., Katoch S., Chauhan S. S. A Review on Genetic Algorithm: Past, Present, and Future. Multimedia Tools and Applications, 2020, 80(4): 8091-8126.

71 Zhang Y. S., Zheng R. C., Shimono K., et al. Effectiveness Testing of a Piezoelectric Energy Harvester for an Automobile Wheel Using Stochastic Resonance. Sensors, 2016, 16(10).

72 Mei X., Zhou S., Yang Z., et al. The benefits of an asymmetric tri-stable energy harvester in low-frequency rotational motion. Applied Physics Express, 2019, 12(5).

73 Xie Z., Kwuimy C. A. K., Wang Z., et al. A piezoelectric energy harvester for broadband rotational excitation using buckled beam. Aip Advances, 2018, 8(1).

74 Malaji P. V., Ali S. F. Analysis and experiment of magneto-mechanically coupled harvesters. Mechanical Systems and Signal Processing, 2018, 108: 304-316.

75 Feng Y.-Y., Chen S.-J., Cheng S.-P. Development of a miniaturized rotational electromagnetic energy harvester with a liquid metal direct-write process. Sensors and Actuators a-Physical, 2019, 295: 224-230.